Journal Pre-proof

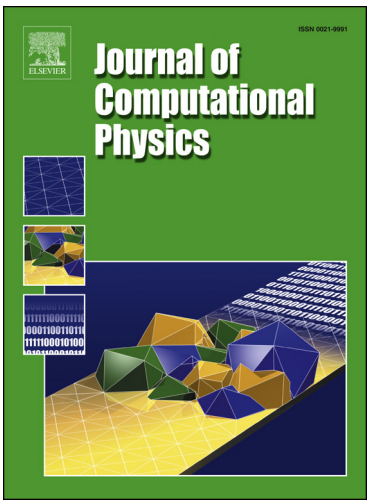

Robust modeling of hysteretic capillary pressure and relative permeability for two phase flow in porous media

Hyun C. Yoon, Peng Zhou, Jihoon Kim

PII: S0021-9991(19)30620-5
DOI: https://doi.org/10.1016/j.jcp.2019.108915
Reference: YJCPH 108915

To appear in: *Journal of Computational Physics*

Received date: 5 June 2018
Revised date: 15 August 2019
Accepted date: 26 August 2019

Please cite this article as: H.C. Yoon et al., Robust modeling of hysteretic capillary pressure and relative permeability for two phase flow in porous media, *J. Comput. Phys.* (2019), 108915, doi: https://doi.org/10.1016/j.jcp.2019.108915.

Highlights

- Numerical simulation of hysteretic capillary pressure and relative permeability.
- Application of plasticity theory to hysteresis in reservoir simulation.
- Mathematical stability analysis of the proposed numerical approach.
- Numerical investigation for cyclic imbibition-drainage processes.

Robust modeling of hysteretic capillary pressure and relative permeability for two phase flow in porous media

Hyun C. Yoon[a], Peng Zhou[a], Jihoon Kim[a]

[a]*Harold Vance Department of Petroleum Engineering, Texas A&M University. 3116 TAMU Richardson Building College Station, TX 77843, USA*

Abstract

We investigate a robust and systematic modeling approach for hysteretic capillary pressure and relative permeability in porous media by using the theory of plasticity, considering that plasticity and hysteresis exhibit both irreversible physical processes. Focusing on the immiscible two-phase flow, we investigate stability analysis and find that the method based on the plasticity can yield well posedness (contractivity) and algorithmic stability (B-stability). This modeling approach can track and compute history-dependent flow properties such as residual saturation. In numerical simulation, we apply the algorithm of the 1D isotropic/kinematic hardening plasticity to reservoir simulation of gas-water flow. For weak and strong capillarity, the modeling yields strong numerical stability even for several drainage-imbibition processes. We also identify differences between with and without hysteresis, showing the importance of hysteretic capillary pressure and relative permeability. Thus, the hysteresis modeling based on the theory of plasticity is promising for robust numerical simulation of strong hysteresis.

Keywords: Hysteresis, Capillary pressure, Relative permeability, Plasticity, Multiphase flow

1. Introduction

Hysteresis in capillary pressure and relative permeability is one of the important physical phenomena in reservoir engineering such as geological CO_2 sequestration, water-alternating gas injection, shale gas development by hydraulic fracturing [1, 2, 3, 4, 5, 6, 7]. Cyclic imbibition and drainage processes in multiple fluid phases such as oil, water, and gas can cause irreversible behavior, which shows history-dependent capillary pressure and relative permeability [8, 9].

Email addresses: benhyoon@tamu.edu (Hyun C. Yoon), qq8588699@tamu.edu (Peng Zhou), jihoon.kim@tamu.edu (Jihoon Kim)

Significant effort has been made to model the hysteretic capillary pressure and relative permeability. For example, at the early stages, Killough [10] proposed a numerical algorithm for the modeling of history-dependent capillary pressure and relative permeability. Juanes et al. [6] investigated the impact of hysteresis in permeability on CO_2 sequestration, and showed the importance of hysteresis modeling. Doughty [11] studied hysteretic relative permeability and capillary pressure with interpolation between main drainage and imbibition curves. Cihan et al. [7] proposed a modeling approach based on distribution of pore-size and connectivity of void space in pore-scale. In soil mechanics, Nuth and Laloui [12] reviewed the modeling of hysteretic capillary pressure within the frame of elastoplasticity in a two phase system within a deformable soil, indicating the analogy between hysteretic capillary pressure and elastoplasticity (i.e. irreversible physics). Pedroso and Williams [13] proposed a different modeling method for capillary hysteresis in the two phase system during the drainage-imbibition processes. In the previous studies of reservoir engineering, researchers have mentioned difficulty in numerical modeling the cyclic imbibition and drainage processes, for example, in CO_2 sequestration, emphasizing importance of the rigorous hysteresis modeling (e.g., Doughty [11]). Compared to other studies, the approach used by Nuth and Laloui [12] is fundamentally based on the plasticity theory, which has been well developed in solid mechanics. Total strain is decomposed into elastic (recoverable) strain and plastic (irrecoverable) strain. Hysteresis also causes reducible and residual (irreducible) saturations. From the similarity, stress and plastic strain correspond to capillary pressures and residual saturation, respectively. Numerically stable return mapping algorithms for modeling plasticity have been proposed and analyzed mathematically and numerically over decades (e.g., Simo and Hughes [14]). The modeling approach yields well-posed mathematical problems for dissipative physical problems, and the return mapping algorithms inherit well posedness algorithmically (i.e., numerical stability). Thus, we can enjoy those methods in modeling hysteresis without significant modification. Still, only few studies have been reported for the modeling of hysteretic capillary pressure and relative permeability for reservoir simulation.

In this study we investigate the modeling of hysteretic capillary pressure and relative permeability for two fluid phases in reservoir simulation. We first construct the equations of the hysteresis modeling, which define the elastic domain, hardening laws, and the plastic flow rule. Then, for the given equations, we use a return mapping algorithm to calculate all the plastic variables in the discretized time domain in this study. We employ

the 1D isotropic and kinematic hardening, and the associative flow rule. Just like elastoplasticity, we define a specific yield function, flow rule, and hardening law, along with the conventional Kuhn-Tucker and consistency conditions. Total saturation is decomposed into elastic and plastic (residual) saturations additively. We then perform in-depth theoretical analysis for the formulation motivated by the plasticity theory. Specifically, we analyze both well posedness (contractivity) and numerical stability (B-stability) with the generalized midpoint rule for $t_{n+\alpha}$, where α is the parameter of time discretization. For numerical simulation, we take a model of hysteretic capillary pressure model used in Nuth and Laloui [12], validated with the experimental results. We present numerical examples with several different cases, and find that the proposed numerical approach is robust and stable even for cyclic imbibition and drainage processes.

2. Mathematical Model

The governing equation for multiphase flow is derived by mass balance as [15]

$$\dot{m}_J + \mathrm{Div}\, \boldsymbol{f}_J = q_J, \tag{1}$$

where $\mathrm{Div}(\cdot)$ is the divergence operator, and the subscript J indicates the fluid phase. m_J is the fluid mass of phase J, and $\dot{(\cdot)}$ means the time derivative (i.e. $\dot{(\cdot)} = dm_J/dt$).

$\boldsymbol{f}_J$ and q_J are mass flow and source terms with a boundary surface Γ on the domain Ω, respectively. The mass flow term can be re-written by Darcy's law, as

$$\boldsymbol{f}_J = \rho_J \boldsymbol{v}_J, \quad \boldsymbol{v}_J = -\frac{\boldsymbol{k}_J}{\mu_J}\left(\mathbf{Grad}\, p_J - \rho_J \boldsymbol{g}\right), \tag{2}$$

where $\rho_J, \boldsymbol{v}_J, \boldsymbol{k}_J, \mu_J, p_J$, and $\boldsymbol{g}$ are density, volumetric fluid velocity, rank-2 positive-definite effective permeability tensor, viscosity, pressure of phase J, and, the gravity vector, respectively. $\boldsymbol{k}_J = \boldsymbol{k} k_{rJ}$, where $\boldsymbol{k}$ and k_{rJ} are the absolute permeability and the relative permeability of phase J, respectively.

The fluid mass of phase J is written by

$$m_J = \phi S_J^t \rho_J, \tag{3}$$

where ϕ is the reservoir porosity, and S_J^t is total saturation of phase J. Then Equation 3 provides

$$\frac{\delta m_J}{\rho_J} = \frac{1}{M_J}\delta p_J + \phi \delta S_J^t, \quad \frac{1}{M_J} = \phi S_J^t c_J, \tag{4}$$

where $\delta(\cdot)$ implies variation of a physical quantity. c_J and S_J^t are the fluid compressibility and total saturation of the phase J, respectively.

We specify initial and boundary conditions for mathematical completeness. For fluid flow we consider the boundary conditions $p_J = \bar{p}_J$ (prescribed pressure) on Γ_p, and $\boldsymbol{v}_J \cdot \boldsymbol{n} = \bar{v}_J$ (prescribed volumetric flux) on Γ_v, where $\boldsymbol{n}$ is the outward unit normal to the boundary, $\partial\Omega$. For well-posedness of the problem, we assume that $\Gamma_p \cap \Gamma_v = \emptyset$, and $\Gamma_p \cup \Gamma_v = \partial\Omega$. The initial condition of the flow problem is $p_J|_{t=0} = p_J^0$ and $S_J|_{t=0} = S_J^0$. The initial pressure and saturation fields should satisfy thermodynamic and hydrodynamic equilibria.

3. Capillary Hysteresis and Plasticity

We can find fundamental similarity between capillary hysteresis and plasticity in geoemechanics [12]. Theory of plasticity relates stress to elastic (recoverable) strain and plastic (irrecoverable) strain. For example, the left of Figure 1 shows an elastoplastic volumetric stress-strain relation under loading (From Points A to C)and unloading (From Points C to D) processes. After the yielding point (Point B), plastic strain occurs during loading (From Points B to C) and does not disappear even after unloading of stress. We can find the similarity in capillary hysteresis, as shown in the right of Figure 1. During the drainage process (from Points P to R), the irreversible process occurs from Points Q to R, causing residual (irrecoverable/irreducible) saturation, while the process from Point P to Q is reversible. Then, during the imbibition process from Points R to S, we identify residual saturation. It is worth noting that plastic strain or residual saturation can only be observed during the unloading or imbibition process, respectively.

Return-mapping is a numerical approach for modeling plasticity. Specifically, for an example of the gas-water system, the theory of plasticity [14] allows us to have the following equations for modeling capillary hysteresis.

$$\text{Definition of capillary pressure: } p_c = p_g - p_w, \tag{5}$$

$$\text{Additive decomposition of total water saturation: } S_w^t = S_w^e + S_w^p, \tag{6}$$

$$\text{Elastic capillary pressure-elastic water saturation relationship: } \dot{p}_c = -E_H \dot{S}_w^e, \tag{7}$$

$$\text{Yield condition: } f_Y = f_Y(-p_c, \kappa) \leq 0, \tag{8}$$

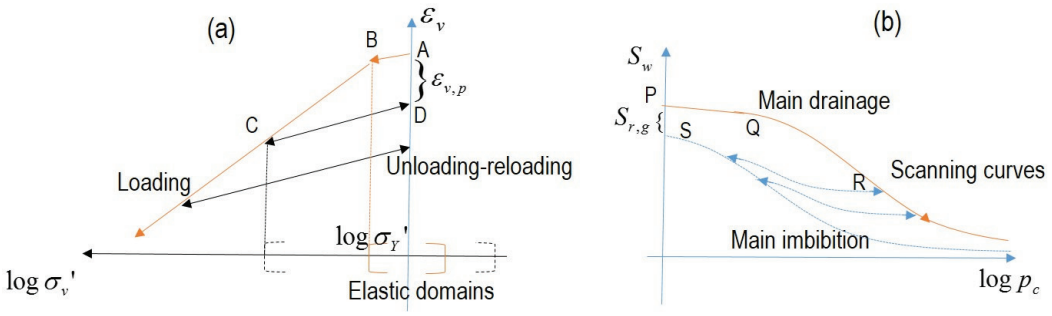

Figure 1: Similarity between plasticity in geomechanics (a) and capillary hysteresis (b). $\sigma_v', \sigma_Y', \varepsilon_v$ **and** $\varepsilon_{v,p}$ **are effective mean stress, effective yield stress, total and plastic volumetric strains, respectively.** $p_c, S_w,$ **and** $S_{r,g}$ **are capillary pressure, water saturation, and residual (irreducible) gas saturation.** $\varepsilon_{v,p}$ **corresponds to** $S_{r,g}$**. The elastic domain of** σ_v' **varies due to hardening.**

$$\text{Relation between hardening variables: } \dot{\kappa} = -H_h \dot{\xi}, \tag{9}$$

$$\text{Plastic flow rule from associative plasticity: } \dot{S}_w^p = \gamma \frac{\partial f_Y}{\partial p_c}, \dot{\xi} = \gamma \frac{\partial f_Y}{\partial \kappa}, \tag{10}$$

$$\gamma f_Y = 0 \text{ (Kuhn-Tucker condition)}, \gamma \dot{f}_Y = 0 \text{ (consistency condition)}, \tag{11}$$

where $S^e, S^p, f_Y, \kappa, \xi, \gamma$ are elastic and plastic saturation, yield function, pressure-like and saturation like hardening variables, and plasticity multiplier, respectively. E_H and H_h are the positive elasticity and hardening moduli, respectively. f_Y is defined as a convex function in the plasticity theory [14]. Then, from Equation 10, we have

$$D_p = \sigma_c \dot{S}_w^p + \kappa \dot{\xi} = (\sigma_c, \kappa) \cdot \left(\dot{S}_w^p, \dot{\xi} \right) \geq 0, \tag{12}$$

where $\sigma_c = -p_c$. The left figure of Figure 2 shows geometrical interpretation of Equation 12.

Furthermore, the associate flow rule based on the maximum plastic dissipation also provides

$$(\pi_c - \sigma_c)\dot{S}_w^p + (\eta - \kappa)\dot{\xi} \leq 0 \quad \text{for } \forall (\pi_c, \eta) \in E, \quad E := \left\{ (\sigma_c, \kappa) \in R \times R,\ \sigma_c, \kappa \in L^2 \right\}, \tag{13}$$

where E is the extended domain of elasticity for the capillary modeling. The geometrical interpretation of Equation 13 is also shown in the right Figure 2.

Note that the additive decomposition of total saturation in Equation 6 implies that we employ the plasticity modeling based on infinitesimal transformation used in geomechanics. Potentially, plastic strain, plastic fluid content, and residual saturation might be related each other in poromechanics [16, 17, 18], although this study

only focuses on the hysteresis modeling for multiphase flow, not being coupled to geomechanics. Thus, it might be required to modify Equation 6 for large deformation of coupled flow and geomechanics where the deformation gradient is decomposed into elastic and plastic parts in a multiplicative way [17, 19].

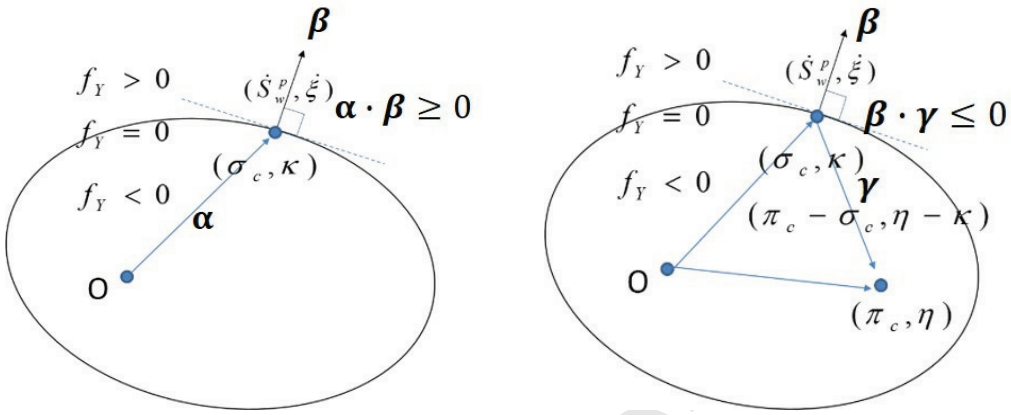

Figure 2: Geometrical interpretation of plastic dissipation (left) and the associative flow rule (right). The yield surface is convex. $\alpha = (\sigma_c, \kappa)$, $\beta = \left(\dot{S}_w^p, \dot{\xi}\right)$, **and** $\gamma = (\pi_c - \sigma_c, \eta - \kappa)$

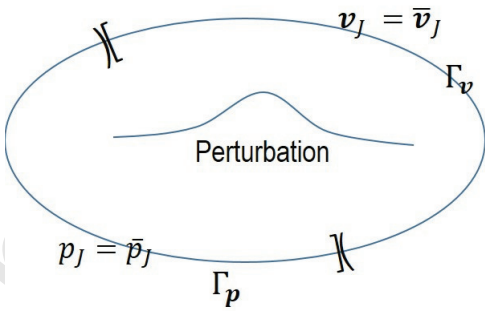

Figure 3: Perturbation introduced in the equilibrated domain.

4. Stability Analysis

We study a-priori estimate of numerical stability, by employing a concept of B-stability [20, 21, 22, 23]. B-stability requires contractivity (well-posedness) and algorithmic stability (numerical stability).

We first consider introducing an initial perturbation within the domain in equilibrium as,

$$^{d}p_j = p_j - \tilde{p}_j,\ ^{d}m_j = m_j - \tilde{m}_j,\ ^{d}S_j = S_j - \tilde{S}_j,$$

where ${}^{d}(\cdot)$ implies the perturbed variables. $(\tilde{\cdot})$ indicates the solutions in equilibrium. From Equation 4, we have

$$\frac{{}^{d}m_g}{\rho_g} = \frac{1}{M_g}\,{}^{d}p_g - \phi\,{}^{d}S_w^t,\ \frac{{}^{d}m_w}{\rho_w} = \frac{1}{M_w}\,{}^{d}p_w + \phi\,{}^{d}S_w^t.$$

The initial values can be considered as perturbation (initial *errors* introduced to the domain), as shown in Figure 3. Then, we investigate evolution of the error in time (stability analysis) for the mathematical statements, given as follows. The flow equations with the *homogeneous* boundary and non-zero initial conditions, assuming an incompressible porous medium, are following:

$$\frac{1}{M_g}\,{}^{d}\dot{p}_g - \phi\,{}^{d}\dot{S}_w^t = \frac{1}{\rho_g}\,\mathrm{Div}\left(\rho_g \frac{\boldsymbol{k}_g}{\mu_g}\,\mathbf{Grad}\ {}^{d}p_g\right),\ \frac{1}{M_g} = \phi S_g^t c_g, \tag{14}$$

$$\frac{1}{M_w}\,{}^{d}\dot{p}_w + \phi\,{}^{d}\dot{S}_w^t = \frac{1}{\rho_w}\,\mathrm{Div}\left(\rho_w \frac{\boldsymbol{k}_w}{\mu_w}\,\mathbf{Grad}\ {}^{d}p_w\right),\ \frac{1}{M_w} = \phi S_w^t c_w, \tag{15}$$

where ϕ is porosity. c_J and S_J^t are the compressibility and total saturation for phase J.

For the stability analysis, let us introduce a norm as follows:

$$||\chi||_T^2 = \frac{1}{2}\int \left(p_g M_g^{-1} p_g + p_w M_w^{-1} p_w + \sigma_c E_h^{-1}\sigma_c + \kappa H_h^{-1}\kappa\right) d\Omega, \tag{16}$$

$$T := \left\{\chi := (p_g, p_w, \sigma_c, \kappa) \in R\times R\times R\times R : p_g, p_w, \sigma_c, \kappa \in L^2(\Omega)\right\},$$

where we have positive correlation between σ_c and S_w^t. Thus, E_h and H_h are positive, characterizing a capillary pressure curve. We will show well-posedness (contractivity) followed by algorithmic stability, written as respectively,

$$\frac{d}{dt}||{}^{d}\chi||_T^2 \le 0,\ \ ||{}^{d}\chi^{n+1}||_T \le ||{}^{d}\chi^{n}||_T. \tag{17}$$

4.1. Contractivity of the Mathematical Problem

From here, we drop the superscript ${}^{d}(\cdot)$ for simplicity (e.g., ${}^{d}\chi \to \chi, {}^{d}p_J \to p_J$). We first take the time derivative of Equation 16, which leads to

$$\begin{aligned}\frac{d}{dt}||\chi||_T^2 &= \int \left(p_g M_g^{-1}\dot{p}_g + p_w M_w^{-1}\dot{p}_w + \sigma_c E_h^{-1}\dot{\sigma}_c + \kappa H_h^{-1}\dot{\kappa}\right)\, d\Omega,\\ &= \int \left(p_g M_g^{-1}\dot{p}_g + p_w M_w^{-1}\dot{p}_w + \sigma_c \dot{S}_w^e - \kappa\dot{\xi}\right)\, d\Omega.\end{aligned} \tag{18}$$

Then, multiply Equation 14 by p_g, we have

$$\int p_g M_g^{-1}\dot{p}_g \, d\Omega - \int p_g \phi \dot{S}_m^t \, d\Omega = \int p_g \frac{1}{\rho_g} \operatorname{Div} \left\{ \rho_g \underbrace{\left(\frac{\boldsymbol{k}_g}{\mu_g} \mathbf{Grad}\, p_g \right)}_{\boldsymbol{v}_g} \right\} d\Omega,$$

$$= \underbrace{\int p_g \boldsymbol{v}_g \cdot \boldsymbol{n} \, d\Gamma}_{=0} - \int \mathbf{Grad}\, p_g \cdot \frac{\boldsymbol{k}_g}{\mu_g} \mathbf{Grad}\, p_g \, d\Omega, \tag{19}$$

where the divergence theorem is applied. The first term of the right hand side is zero due to the homogeneous boundary condition. Similarly, Equation 15 yields

$$\int p_w M_w^{-1}\dot{p}_w \, d\Omega + \int p_w \phi \dot{S}_w^t \, d\Omega = 0 - \int \mathbf{Grad}\, p_w \cdot \frac{\boldsymbol{k}_w}{\mu_w} \mathbf{Grad}\, p_w \, d\Omega. \tag{20}$$

Also, Equations 6 and 12 provide

$$\sigma_c \dot{S}_w^e - \kappa\dot{\xi} = \sigma_c \dot{S}_w^t - \sigma_c \dot{S}_w^p - \kappa\dot{\xi} = \sigma_c \dot{S}_w^t - \underbrace{D_p}_{\geq 0}. \tag{21}$$

Then, we have

$$\begin{aligned}
\frac{d}{dt}||\chi||_T^2 &= \int \left(p_g M_g^{-1}\dot{p}_g + p_w M_w^{-1}\dot{p}_w + \sigma_c \dot{S}_w^e - \kappa\dot{\xi} \right) d\Omega \\
&= -\int \mathbf{Grad}\, p_g \cdot \frac{\boldsymbol{k}_g}{\mu_g} \mathbf{Grad}\, p_g \, d\Omega + \int p_g \phi \dot{S}_w^t \, d\Omega - \int \mathbf{Grad}\, p_w \cdot \frac{\boldsymbol{k}_w}{\mu_w} \mathbf{Grad}\, p_w \, d\Omega \\
&\quad - \int p_w \phi \dot{S}_w^t \, d\Omega + \int \left(\sigma_c \dot{S}_w^e - \kappa\dot{\xi} \right) d\Omega \\
&= -\int \mathbf{Grad}\, p_g \cdot \frac{\boldsymbol{k}_g}{\mu_g} \mathbf{Grad}\, p_g \, d\Omega - \int \mathbf{Grad}\, p_w \cdot \frac{\boldsymbol{k}_w}{\mu_w} \mathbf{Grad}\, p_w \, d\Omega - \int \sigma_c \phi \dot{S}_w^t \, d\Omega \\
&\quad + \int \left(\sigma_c \underbrace{\dot{S}_w^e}_{\dot{S}_w^t - \dot{S}_w^p} - \kappa\dot{\xi} \right) d\Omega \\
&= -\int \mathbf{Grad}\, p_g \cdot \frac{\boldsymbol{k}_g}{\mu_g} \mathbf{Grad}\, p_g \, d\Omega - \int \mathbf{Grad}\, p_w \cdot \frac{\boldsymbol{k}_w}{\mu_w} \mathbf{Grad}\, p_w \, d\Omega \\
&\quad - \int \left(\sigma_c \dot{S}_w^p + \kappa\dot{\xi} \right) d\Omega + \int \sigma_c \left(1-\phi\right) \dot{S}_w^t \, d\Omega \\
&\leq 0.
\end{aligned} \tag{22}$$

Thus, the proposed formulation provides a well-posed problem (contractivity).

4.2. B-Stability

A numerical algorithm is B-stable when, for a given contractive problem, it provides numerical (algorithm) stability. We employ the generalized mid-point rule in time discretization. Then,

$$M_g^{-1}\frac{p_g^{n+1}-p_g^n}{\Delta t}-\phi\frac{S_w^{t,n+1}-S_w^{t,n}}{\Delta t}=\frac{1}{\rho_g}\,\mathrm{Div}\left(\frac{\boldsymbol{k}_g}{\mu_g}\,\mathbf{Grad}\,p_g^{n+\alpha}\right), \tag{23}$$

$$M_w^{-1}\frac{p_w^{n+1}-p_w^n}{\Delta t}+\phi\frac{S_w^{t,n+1}-S_w^{t,n}}{\Delta t}=\frac{1}{\rho_w}\,\mathrm{Div}\left(\frac{\boldsymbol{k}_w}{\mu_w}\,\mathbf{Grad}\,p_w^{n+\alpha}\right), \tag{24}$$

$$p_J^{n+\alpha}=\alpha p_J^{n+1}+(1-\alpha)\,p_J^n,$$

where Δt is the time step size and α is the parameter of time discretization.

Let us multiply Equation 23 by $p_g^{n+\alpha}$, which yields

$$\begin{aligned}&\int p_g^{n+\alpha}M_g^{-1}\frac{p_g^{n+1}-p_g^n}{\Delta t}\,d\Omega-\int p_g^{n+\alpha}\phi\frac{S_w^{t,n+1}-S_w^{t,n}}{\Delta t}\,d\Omega,\\&=\int p_g^{n+\alpha}\frac{1}{\rho_g}\,\mathrm{Div}\left(\frac{k_g}{\mu_g}\,\mathbf{Grad}\,p_g^{n+\alpha}\right)\,d\Omega,\\&=0-\int\frac{1}{\rho_g}\,\mathbf{Grad}\,p_g^{n+\alpha}\cdot\frac{k_g}{\mu_g}\,\mathbf{Grad}\,p_g^{n+\alpha}\,d\Omega.\end{aligned} \tag{25}$$

We also introduce the following identity,

$$\int p_g^{n+\alpha}M_g^{-1}\frac{p_g^{n+1}-p_g^n}{\Delta t}\,d\Omega=\frac{1}{2}M_g^{-1}\left(||p_g^{n+1}||_{L^2}^2-||p_g^n||_{L^2}^2\right)+(2\alpha-1)\frac{1}{2}M_g^{-1}||p_g^{n+1}-p_g^n||_{L^2}^2. \tag{26}$$

Then, from Equation 25 and 26, we have

$$\begin{aligned}&\frac{1}{2}M_g^{-1}\left(||p_g^{n+1}||_{L^2}^2-||p_g^n||_{L^2}^2\right)+(2\alpha-1)\frac{1}{2}M_g^{-1}||p_g^{n+1}-p_g^n||_{L^2}^2-\int p_g^{n+\alpha}\phi\frac{S_w^{t,n+1}-S_w^{t,n}}{\Delta t}\,d\Omega\\&=-\int\frac{1}{\rho_g}\,\mathbf{Grad}\,p_g^{n+\alpha}\cdot\frac{k_g}{\mu_g}\,\mathbf{Grad}\,p_g^{n+\alpha}\,d\Omega.\end{aligned} \tag{27}$$

Similarly, Equation 24 can be written as

$$\begin{aligned}&\frac{1}{2}M_w^{-1}\left(||p_w^{n+1}||_{L^2}^2-||p_w^n||_{L^2}^2\right)+(2\alpha-1)\frac{1}{2}M_w^{-1}||p_w^{n+1}-p_w^n||_{L^2}^2+\int p_w^{n+\alpha}\phi\frac{S_w^{t,n+1}-S_w^{t,n}}{\Delta t}\,d\Omega\\&=-\int\frac{1}{\rho_w}\,\mathbf{Grad}\,p_w^{n+\alpha}\cdot\frac{k_w}{\mu_w}\,\mathbf{Grad}\,p_w^{n+\alpha}\,d\Omega.\end{aligned} \tag{28}$$

Then, adding Equation 27 and 28, we have

$$\begin{aligned}
&\frac{1}{2}M_g^{-1}\left(||p_g^{n+1}||_{L^2}^2-||p_g^n||_{L^2}^2\right)+\frac{1}{2}M_w^{-1}\left(||p_w^{n+1}||_{L^2}^2-||p_w^n||_{L^2}^2\right)+\int\sigma_c^{n+\alpha}\phi\frac{S_w^{t,n+1}-S_w^{t,n}}{\Delta t}\,d\Omega\\
&=-\int\frac{1}{\rho_g}\,\mathbf{Grad}\,p_g^{n+\alpha}\cdot\frac{k_g}{\mu_g}\,\mathbf{Grad}\,p_g^{n+\alpha}\,d\Omega-\int\frac{1}{\rho_w}\,\mathbf{Grad}\,p_w^{n+\alpha}\cdot\frac{k_w}{\mu_w}\,\mathbf{Grad}\,p_w^{n+\alpha}\,d\Omega\\
&\quad-(2\alpha-1)\frac{1}{2}M_g^{-1}||p_g^{n+1}-p_g^n||_{L^2}^2-(2\alpha-1)\frac{1}{2}M_w^{-1}||p_w^{n+1}-p_w^n||_{L^2}^2.
\end{aligned}\tag{29}$$

The return mapping with the generalized mid-point rule and associative plasticity (i.e., the algorithmic counterpart of Equation 12) satisfies

$$\begin{aligned}
D_p&=\sigma_c^{n+\alpha}(S_w^{p,n+1}-S_w^{p,n})+\kappa^{n+\alpha}(\xi^{n+1}-\xi^n)\geq 0,\\
\sigma_c^{n+\alpha}&=\alpha\sigma_c^{n+1}+(1-\alpha)\sigma_c^n,\ \kappa^{n+\alpha}=\alpha\kappa^{n+1}+(1-\alpha)\kappa^n.
\end{aligned}\tag{30}$$

Then, integrating Equation 30 over the domain and multiply the equation by -1, we obtain

$$-\int\sigma_c^{n+\alpha}\left(S_w^{t,n+1}-S_w^{t,n}\right)\,d\Omega+\int\sigma_c^{n+\alpha}\left(S_w^{e,n+1}-S_w^{e,n}\right)\,d\Omega-\int\kappa^{n+\alpha}\left(\xi^{n+1}-\xi^n\right)\,d\Omega\leq 0.\tag{31}$$

Considering the discretization of Equation 7 and 9 written as,

$$\sigma_c^{n+1}-\sigma_c^n=E_h(S_w^{e,n+1}-S_w^{e,n}),\ \kappa^{n+1}-\kappa^n=-H_h(\xi^{n+1}-\xi^n),\tag{32}$$

Equation 31 yields

$$\begin{aligned}
&-\int\sigma_c^{n+\alpha}\left(S_w^{t,n+1}-S_w^{t,n}\right)\,d\Omega+\frac{1}{2}\int\sigma_c^{n+1}E_h^{-1}\sigma_c^{n+1}\,d\Omega-\frac{1}{2}\int\sigma_c^nE_h^{-1}\sigma_c^n\,d\Omega\\
&+\frac{1}{2}\int\kappa^{n+1}H_h^{-1}\kappa^{n+1}\,d\Omega-\frac{1}{2}\int\kappa^nH_h^{-1}\kappa^n\,d\Omega\\
&\leq-(2\alpha-1)\frac{E_h^{-1}}{2}||\sigma_c^{n+1}-\sigma_c^n||_{L^2}^2-(2\alpha-1)\frac{H_h^{-1}}{2}||\kappa^{n+1}-\kappa^n||_{L^2}^2.
\end{aligned}\tag{33}$$

As a result, combining Equations 28, 29, and 33, we show

$$\begin{aligned}
\left(||\chi^{n+1}||_T\right)^2-\left(||\chi^n||_T\right)^2=&\frac{1}{2}M_g^{-1}\left(||p_g^{n+1}||_{L^2}^2-||p_g^n||_{L^2}^2\right)+\frac{1}{2}M_w^{-1}\left(||p_w^{n+1}||_{L^2}^2-||p_w^n||_{L^2}^2\right)+\\
&\frac{1}{2}E_h^{-1}\left(||\sigma_c^{n+1}||_{L^2}^2-||\sigma_c^n||_{L^2}^2\right)+\frac{1}{2}H_h^{-1}\left(||\kappa^{n+1}||_{L^2}^2-||\kappa^n||_{L^2}^2\right)\\
\leq&-\int\frac{1}{\rho_g}\,\mathbf{Grad}\,p_g^{n+\alpha}\cdot\frac{k_g}{\mu_g}\,\mathbf{Grad}\,p_g^{n+\alpha}\,d\Omega\\
&-\int\frac{1}{\rho_w}\,\mathbf{Grad}\,p_w^{n+\alpha}\cdot\frac{k_w}{\mu_w}\,\mathbf{Grad}\,p_w^{n+\alpha}\,d\Omega\\
&-(2\alpha-1)\frac{M_g^{-1}}{2}||p_g^{n+1}-p_g^n||_{L^2}^2-(2\alpha-1)\frac{M_w^{-1}}{2}||p_w^{n+1}-p_w^n||_{L^2}^2\\
&-(2\alpha-1)\frac{E_h^{-1}}{2}||\sigma_c^{n+1}-\sigma_c^n||_{L^2}^2-(2\alpha-1)\frac{H_h^{-1}}{2}||\kappa^{n+1}-\kappa^n||_{L^2}^2.
\end{aligned}\tag{34}$$

Thus, we have B-stability for $0.5 \leq \alpha \leq 1$. The B-stable algorithm is thermodynamically consistent in the sense that its solution complies with the second law of thermodynamics, dissipative character [24].

5. Hysteresis Modeling of Capillary Pressure and Relative Permeability

In this study, we employ a hysteresis model for capillary pressure used in Nuth and Laloui [12], based on application of one dimensional plasticity with kinematic hardening [14], focusing on the two phase flow system (e.g., gas and water). We specifically have a yield function of

$$f_Y = |\log p_c - \log q + \sigma_Y| - \sigma_Y \leq 0,\ \sigma_Y = \frac{1}{2}(\log q_0 - \log p_{eH}), \tag{35}$$

where p_{eH} is the entry pressure. The elastic modulus, hardening relation and plastic flow followed by the plastic multiplier are given respectively as

$$E_h = K_h \frac{p_c}{p_{eH}},\ \frac{\dot{q}}{q} = B_H \gamma \frac{\partial f_Y}{\partial q},\ \dot{S}_w^p = \gamma \frac{\partial f_Y}{\partial p_c},\ \gamma = \frac{\dot{p}_c}{B_H} \text{sign}(\log p_c - \log q + \sigma_Y), \tag{36}$$

where K_h is a positive modulus that characterizes E_H, and q is a pressure-like hardening variable. σ_Y is a constant that limits the elastic domain. B_H is the coefficient of compressibility for the plastic part of degree of saturation:

$$q = q_0 \cdot \exp(B_H S_w^p). \tag{37}$$

Then, from Equations 35 and 36, the elastoplastic tangent modulus (E_T) can be calculated as follows.

$$E_T \left(= \frac{d\sigma_c}{dS_w^t} = -\frac{dp_c}{dS_w^t} \right) = \frac{p_c}{\frac{p_{eH}}{K_h} + \frac{1}{B_H}} \Leftrightarrow -\frac{d \log p_c}{dS_w^t} = \frac{1}{\frac{p_{eH}}{K_h} + \frac{1}{B_H}} \tag{38}$$

Note that the plastic water saturation corresponds to the residual gas saturation in the capillary pressure curve, as shown in Figure 1. For the modeling of relative permeability, we assume that the residual saturation of gas can be related to plastic water saturation, as follows.

$$k_{rg}\left(S_g^t, S_{rg}\right), S_{rg} = \psi S_w^p, \tag{39}$$

where ψ is a factor that indicates the difference between capillary pressure and relative permeability for the residual saturation. From Pruess et al. [25], ψ is recommended to be slightly less than unity. We use the

modified version of Stone's relative permeability model, written as

$$k_{rg} = \max\left\{0, \min\left\{\left(\frac{S_g^t - S_{rg}}{1 - S_{rw}}\right)^{n_g}, 1\right\}\right\}, \; k_{rw} = \max\left\{0, \min\left\{\left(\frac{S_w^t - S_{rw}}{1 - S_{rw}}\right)^{n_g}, 1\right\}\right\}, \tag{40}$$

where we take $n_g = 4$ and $\psi = 1.0$ unless noted otherwise. Then, return mapping algorithm is applied to model the drainage and imbibition process with the details given in Table 5. For particular ranges of capillary pressure and saturation, within the saturated state ($p_c < p_{eH}$) on the one hand and the residual saturation state ($S_w = S_{rw}$) on the other hand, the elastic increment remains null, and the degree of saturation equals either $1 - S_{rg}$ or S_{rw}, respectively.

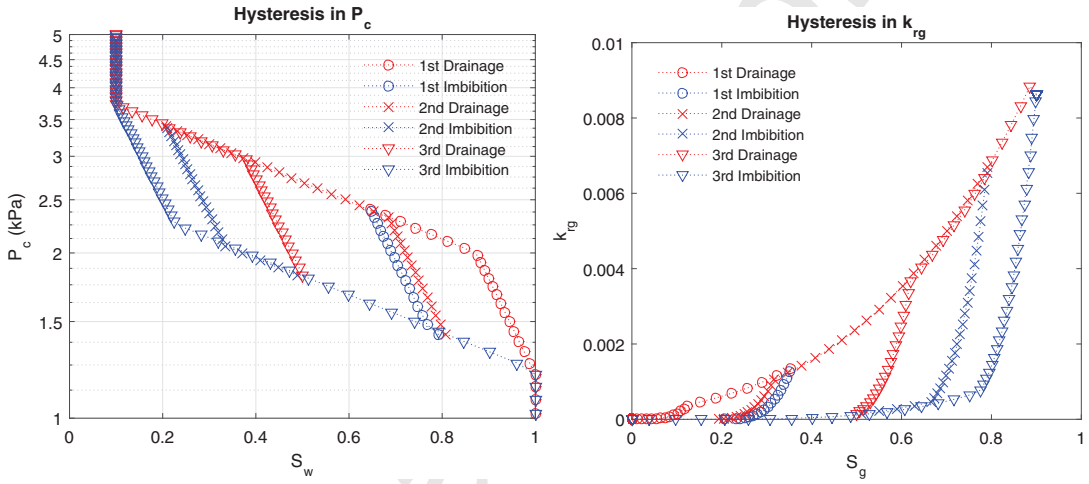

Figure 4: Hysteresis by the drainage-imbibition process in a single gridblock by arbitrarily changing the capillary pressure (Algorithm I). Left: capillary pressure. Right: relative permeability of gas. The algorithm provides numerical stability.

When the fully implicit method is taken with the Newton-Raphson method, p_c^{n+1} is updated every iteration. As a result, the return mapping is invoked every iteration, too. The algorithm of Table 5 is based on the given capillary pressure field (e.g., the case where the flow problem takes the primary variables of p_g and p_w). When the saturation field is given (e.g., the case where the primary variables are p_g and S_w^t), we can easily modify the procedure of the return mapping, shown in Table 2, which corresponds to the 1D isotropic/kinematic hardening in Simo and Hughes [14] after taking the logarithms of p_c and q.

In this study, the reservoir is initially saturated mostly with water, assuming the constant maximum residual water saturation. This return algorithm can straightforwardly be applied to the opposite case where the reservoir is initially saturated mostly with gas, assuming the constant maximum residual gas saturation and calculating

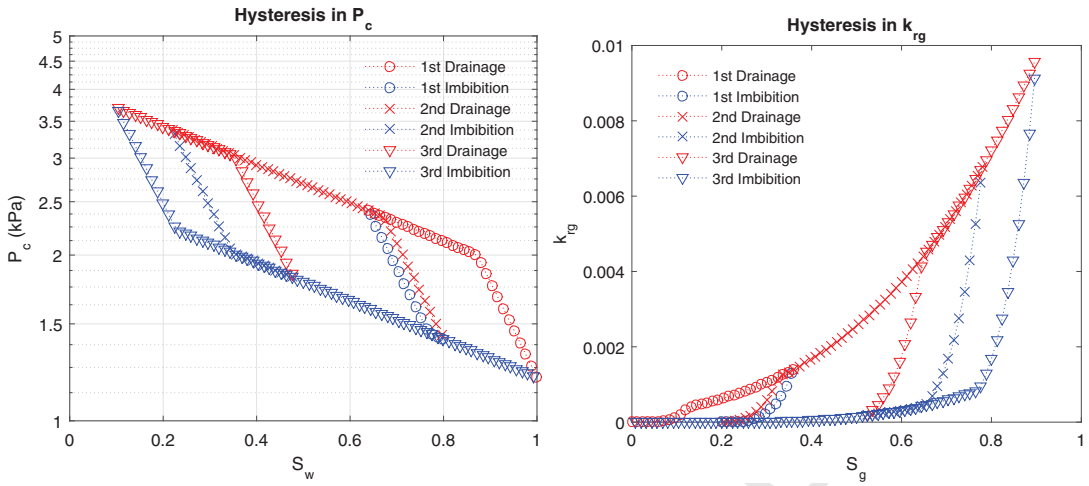

Figure 5: Hysteresis by the drainage-imbibition process in a single gridblock by arbitrarily changing the total gas saturation (Algorithm II). Left: capillary pressure. Right: relative permeability of gas. The algorithm provides numerical stability.

Table 1: Algorithm I of the return mapping for hysteretic capillary pressure and relative permeability

1. Given the capillary pressure field at the n+1 time step: $p_c^{n+1} = p_c^n + \Delta p_c^n$,

2. Compute $f_Y^{trial} = |\log p_c^{n+1} - \log q^n + \sigma_Y| - \sigma_Y$,

$$S_w^{trial} = S_w^n - \frac{\Delta p_c^n}{K_h\left(p_c^{n+1}/p_{eH}\right)}.$$

3. If $f_Y^{trial} \leq 0$, then

Elastic step: $S_w^{n+1} = S_w^{trial}$, $S_w^{p,n+1} = S_w^{p,n}$, $q^{n+1} = q^n$.

Else

Plastic step: proceed to Step 4.

4. Return mapping

$$S_w^{n+1} = S_w^{trial} - \frac{\Delta p_c^n}{B_H p_c^{n+1}},$$

$$S_w^{p,n+1} = S_w^{p,n} + \frac{\Delta p_c^n}{B_H p_c^{n+1}},$$

$$q^{n+1} = q_0 \cdot \exp(B_H S_w^{p,n+1}).$$

5. Update relative permeability: $k_{rg}^{n+1}\left(S_g^{t,n+1}, S_{rg}^{n+1}\right)$, $S_{rg}^{n+1} = \psi S_w^{p,n+1}$.

dynamic residual water saturation. One might also be able to extend this algorithm to the case for both dynamic residual gas and water saturations, which will be part of the future study. Also, without significant modification, the return mapping algorithm of 1D isotropic/kinematic hardening can potentially be applied to Brooks-Corey and van Genuchten models [26, 27, 28], although the elastic and elastoplastic moduli are not constant but calculated from capillary pressure at the previous step due to nonlinearity.

Table 2: Algorithm II of the return mapping for hysteretic capillary pressure and relative permeability

1. Given the saturation field at the n+1 time step: $S_w^{t,n+1} = S_w^{t,n+1} + \Delta S_w^{t,n}$,

2. Compute the trial variables:

$$\log p_c^{trial} = \log p_c^n - \frac{K_h}{p_{eH}} \Delta S_w^{t,n},$$

$$\log q^{trial} = \log q^n,$$

$$\zeta^{trial} = \log p_c^{trial} - \log q^{trial},$$

$$f_Y^{trial} = |\zeta^{trial} + \sigma_Y| - \sigma_Y.$$

3. If $f_Y^{trial} \leq 0$, then

Elastic step: $\log p_c^{n+1} = \log p_c^{trial}$, $q^{n+1} = q^{trial}$, $S_w^{p,n+1} = S_w^{p,n}$.

Else

Plastic step: proceed to Step 4.

4. Return mapping

$$\log p_c^{n+1} = \log p_c^{trial} - \frac{f_Y^{trial}}{\frac{K_h}{p_{eH}} + B_H} \frac{K_h}{p_{eH}} \text{sign}(\zeta^{trial}),$$

$$\log q^{n+1} = \log q^{trial} + \frac{f_Y^{trial}}{\frac{K_h}{p_{eH}} + B_H} B_H \text{sign}(\zeta^{trial}),$$

$$S_w^{p,n+1} = S_w^{p,n} + \frac{f_Y^{trial}}{\frac{K_h}{p_{eH}} + B_H} \text{sign}(\zeta^{trial}),$$

5. Update relative permeability: $k_{rg}^{n+1}\left(S_g^{t,n+1}, S_{rg}^{n+1}\right)$, $S_{rg}^{n+1} = \psi S_w^{p,n+1}$.

Figures 4 and 5 show the numerical results of capillary pressure and relative permeability for the cyclic drainage-imbibition processes by arbitrarily changing the capillary pressure (Algorithm I) and the total gas saturation (Algorithm II), respectively. In this test case we have $p_{eH} = 1.2kPa$, $q_0 = 2.0kPa$, $K_h = 4.8kPa$, and $B_H = 1.0Pa$. We take constant residual water saturation, $S_{rw} = 0.1$. Even though the drainage and imbibition processes are changed repeatedly and significantly, we identify that the numerical algorithms based

on the plasticity theory are stable for the hysteretic modeling. Figure 6 shows the extended elastic domain of σ_c and κ, which corresponds to Equation 35. We identify that the extended elastic domain is convex as well as that the evolution of σ_c and κ occurs within the extended elastic domain.

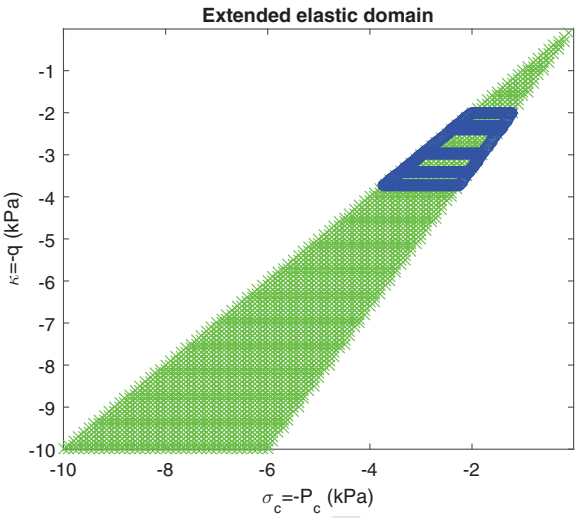

Figure 6: The extended elastic domain, which corresponds to Equation 35, colored in green. The blue line indicates the evolution of σ_c and κ during the cyclic drainage-imbibition processes.

6. Numerical Examples

We perform several numerical experiments in order to investigate stability and robustness of the proposed hysteresis modeling method. We consider an isothermal flow problem in a 1D horizontal reservoir to show the hysteresis effect in capillary pressure and relative permeability on multiphase flow. We take the finite volume method for space discretization [15]. The domain is uniformly discretized with 60 gridblocks, where the gridblock sizes are uniform, ($\Delta x = 4m$, $\Delta y = 10m$, $\Delta z = 10m$) and the length of the domain is $L_x = 240m$. We take no-flow boundary conditions at both sides, as shown in Figure 7. The permeability and porosity are 3.0×10^{-15} m^2 and 0.1, respectively. We take the backward Euler method (i.e., $\alpha = 1.0$). We use the Peng-Robinson equation to solve the equation of state for gas, which determines gas properties such as viscosity and compressibility. We take the properties of water defined at given reservoir pressure and temperature.

Methane gas (CH_4) and liquid water are injected continuously and successively into the reservoir in order to model the drainage and imbibition processes. The simulation time is 70 days. Initial saturations of gas and

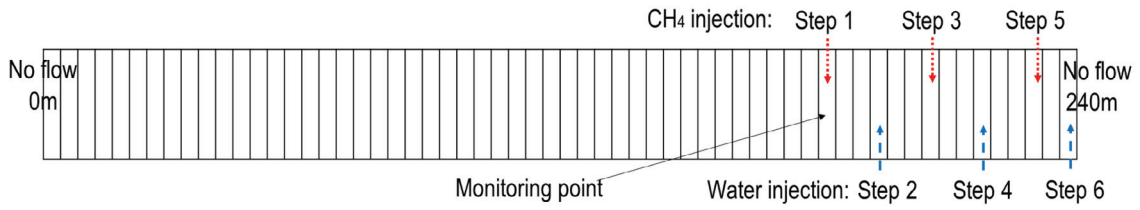

Figure 7: Illustration of the 1D reservoir, boundary conditions, source, and monitoring point locations.

water are $S_g = 0.1$ and $S_w = 0.9$, respectively. We take initial gas pressure of $p_g = 10MPa$ and temperature of $T = 20^oC$, respectively. We take a monitoring point located at $x = 182m$ to observe variation of the saturation and capillary pressure. The entire simulation is divided into six steps (Figure 7) as follows:

1. A first CH_4 injection (0.3kg/s for 2 days) in the element at ($x = 182m$) for the first drainage
2. A first H_2O injection (0.02kg/s for 23 days) in the element ($x = 194m$) for the first imbibition
3. A second CH_4 injection (0.05kg/s for 10 days) in the element at ($x = 206m$) for the second drainage
4. A second H_2O injection (0.01kg/s for 20 days) in the element ($x = 218m$) for the second imbibition
5. A third CH_4 injection (0.02kg/s for 10 days) in the element at ($x = 230m$) for the third drainage
6. A third H_2O injection (0.01kg/s for 5 days) in the element ($x = 238m$) for the third imbibition

With the drainage and imbibition cycles of the six steps, we investigate the effects of hysteresis in capillary pressure and relative permeability with 6 different test cases, considering weak and strong capillarity. Cases 1, 2, 3, and 6 have weak capillarity while Cases 4 and 5 have strong capillarity (See Table 3).

Specifically, Cases 1, 2, 3, and 6 take $p_{eH} = 1.5kPa$, $q_0 = 4.0kPa$, $E_H = 15.0kPa$, and $B_H = 1.0Pa$, while Cases 4 and 5 have $p_{eH} = 1.5MPa$, $q_0 = 4.0kPa$, $E_H = 15.0MPa$, and $B_H = 1.0Pa$. Initial residual saturations of gas and water are $S_{rg} = 0.0$ and $S_{rw} = 0.15$, respectively. The specific values of the parameters of p_{eH}, E_H, and q_0 are summarized in Table 3.

Those cases are separated by the different scenarios in hysteresis. For example, we consider hysteresis effects in both capillary pressure and relative permeability for Case 1, while only hysteresis in capillary pressure is considered for Case 2. Case 3 takes neither hysteretic capillary pressure nor relative permeability. Only Case 6 takes $n_g = 2$ for Equation 40, while all the other cases take $n_g = 4$. We take Case 1 as a reference case. Table 4 summarizes the six different scenarios.

Table 3: Parameters of capillary pressure

	Case 1	Case 2	Case 3	Case 6	Case 4	Case 5
Parameters	Weak capillarity				Strong capillarity	
p_{eH}	1.5 kPa				1.5 MPa	
E_H	15.0 kPa				15.0 MPa	
q_0	4.0 kPa				4.0 MPa	

Table 4: Six different scenarios. O: Hysteresis, X: No hysteresis

	Capillary Pressure	Relative Permeability
Case 1	O	O
Case 2	O	X
Case 3	X	X
Case 4	O	O
Case 5	O	X
Case 6	O	O

6.1. Hysteresis in capillary pressure and relative permeability

Figures 8 and 9 show dynamic capillary pressure and relative permeability at the monitoring point for Cases 1 (reference case), 2, and 3. For those cases, we identify cyclic drainage and imbibition processes from Step 1 through Step 6. For the reference case, we find that the modelings of hysteretic capillary pressure and relative permeability are stable even for the complex drainage and imbibition processes.

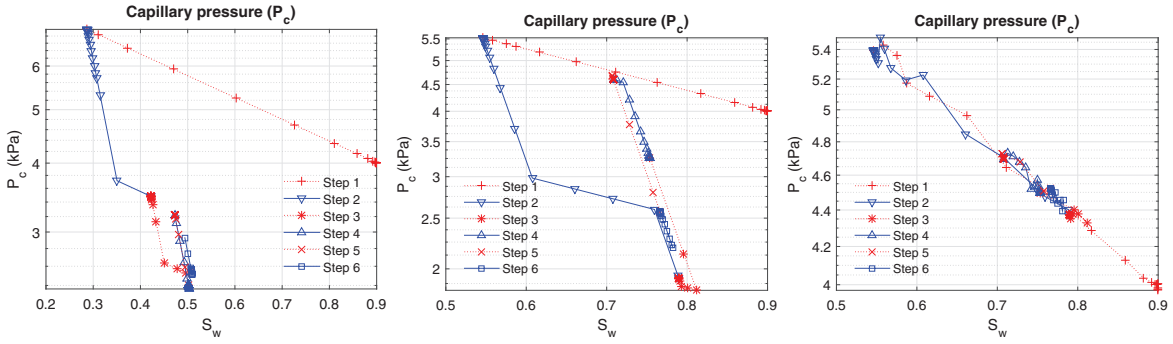

Figure 8: Evolution of capillary pressure for the reference case (left), Case 2 (center), and Case 3 (right).

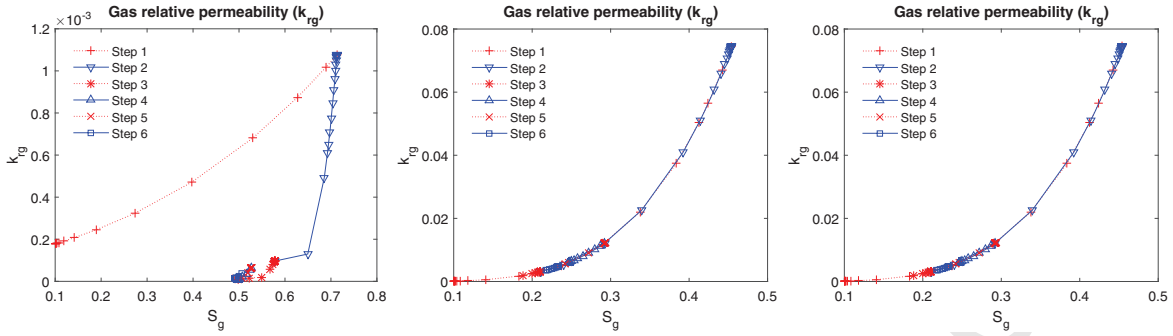

Figure 9: Evolution of gas relative permeability for the reference case (left), Case 2 (center), and Case 3 (right).

Even when the relative permeability of gas is zero, the residual saturation of gas can decrease (the left of Figure 9) due to mass influx of water into the gridblock. For Case 2, the behavior of capillary pressure is different from that of the reference case, because only hysteretic capillary pressure is considered, not hysteretic relative permeability.

The relative permeability significantly affects the flow regime. From Figures 10 and 11, we identify the considerable differences in gas pressure and water saturation between the reference case and Case 2, while the results of gas pressure and water saturation between Cases 2 and 3 are almost identical. This implies an important role of relative permeability in multiphase flow. For capillary pressure, we find different distributions and evolutions for all three cases.

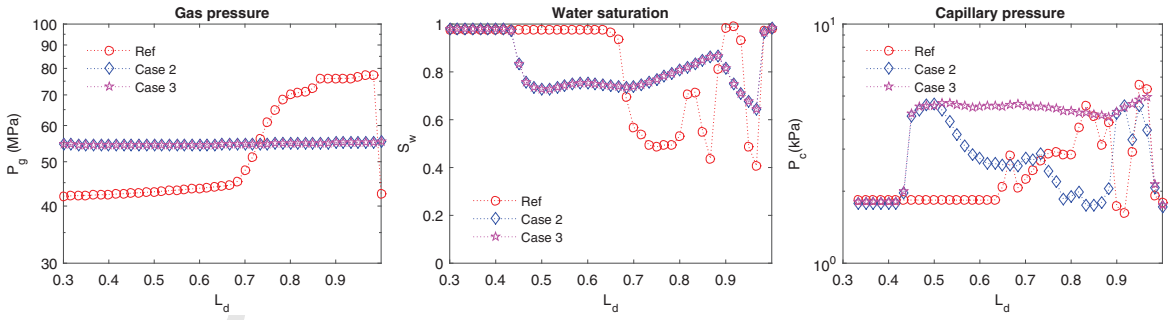

Figure 10: Distribution of gas pressure (left), water saturation (center), and capillary pressure (right) after Step 6 for the reference case, Cases 2 and 3. 'Ref' indicates the reference case. $L_d = x/L_x$ **is a normalized distance.**

6.2. Effect of strong capillarity

We further investigate the modeling capability of hysteresis for strong capillarity. In Cases 4 and 5, from Figure 12, we find numerical stability of strong hysteretic capillary pressure, where the capillary pressure in-

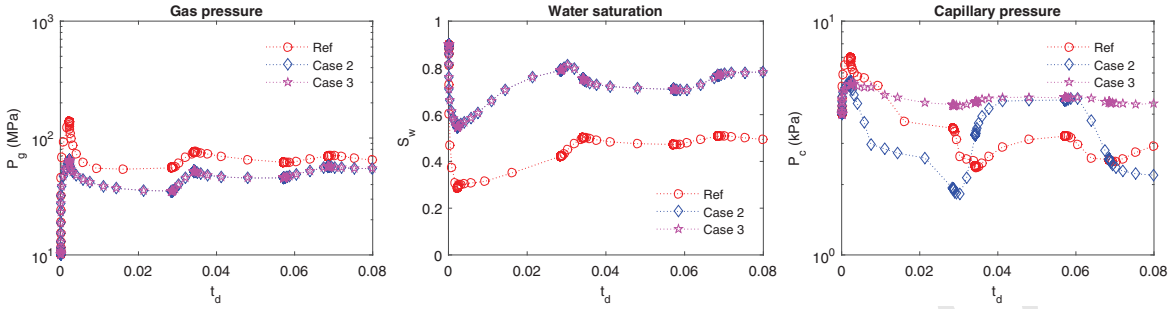

Figure 11: Evolution of gas pressure (left), water saturation (center), and capillary pressure (right) at the monitoring point for the reference case, Case 2, and Case 3. $t_d = \frac{\bar{Q}_f}{M_t} t$ is a normalized time, where $\bar{Q}_f$ and M_t are the average mass rate of injection and the original total mass of fluid in the reservoir, respectively.

creases up to 10 MPa. Figure 13 shows evolutions with and without hysteresis in gas relative permeability when the hysteresis of strong capillary pressure is considered, which corresponds to Figure 12. These results show numerical stability in the relative permeability field, too.

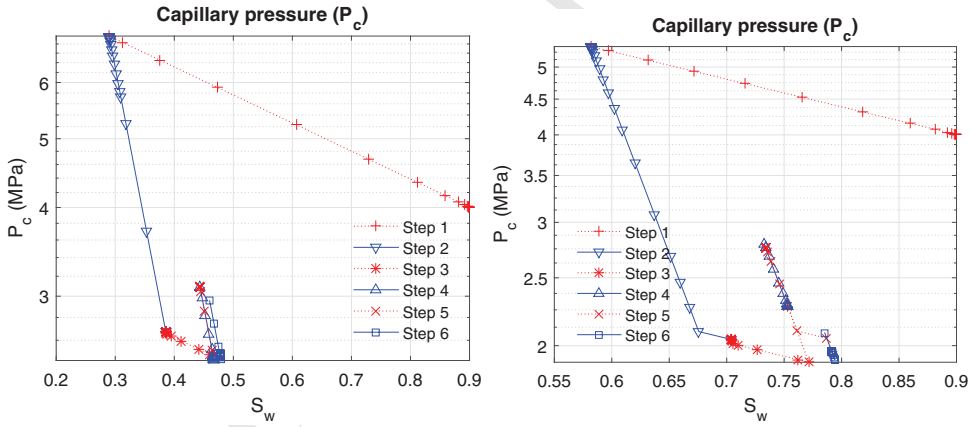

Figure 12: Evolution of strong capillary pressure for Case 4 (left) and Case 5 (right).

Figure 14 shows spatial distributions of gas pressure, water saturation, and capillary pressure after Step 6 for Cases 4 and 5 as well as the reference case. The behavior of relative permeability in Case 4 (the left of Figure 13) is almost identical to that in the reference case. Thus, the distributions of gas pressure and water saturation of Case 4 are almost same as those of the reference case, although the distribution of the capillary pressure is different. Similarly, shown in Figure 15, evolutions of gas pressure and water saturation at the monitoring point between Case 4 and the reference case are almost identical, while those of capillary pressure are different. From the results of both weak and strong capillarity cases, the capillary hysteresis changes residual gas saturation

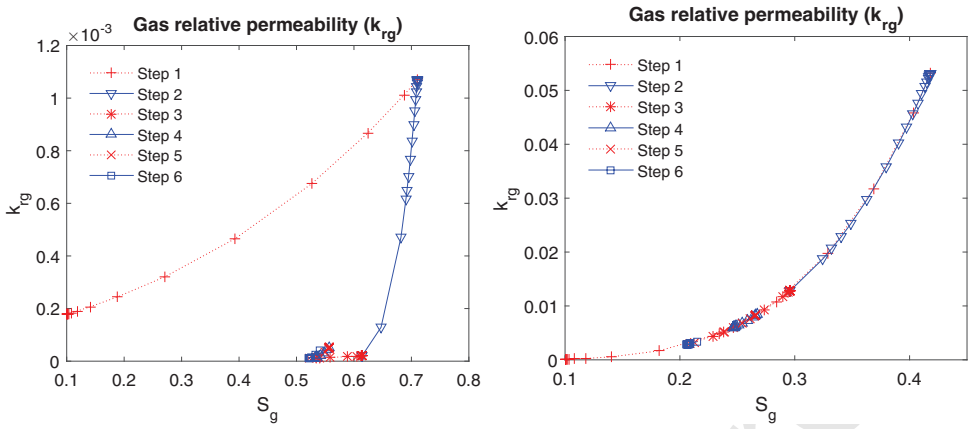

Figure 13: Evolution of gas relative permeability for Case 4 (left) and Case 5 (right), which corresponds to Figure 12.

dynamically. When the dynamic residual saturation is reflected in relative permeability, it alters the flow regime significantly, affecting the fields of pressure and saturation.

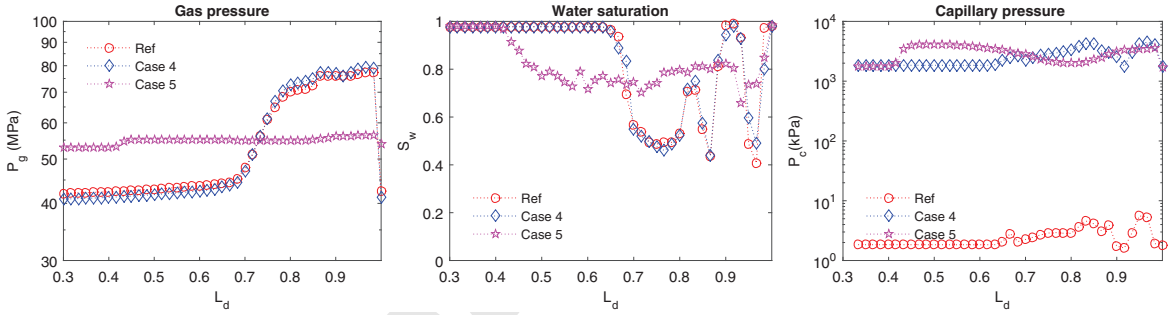

Figure 14: Distribution of gas pressure (left), water saturation (center), and capillary pressure (right) after Step 6 for the reference case, Cases 4 and 5.

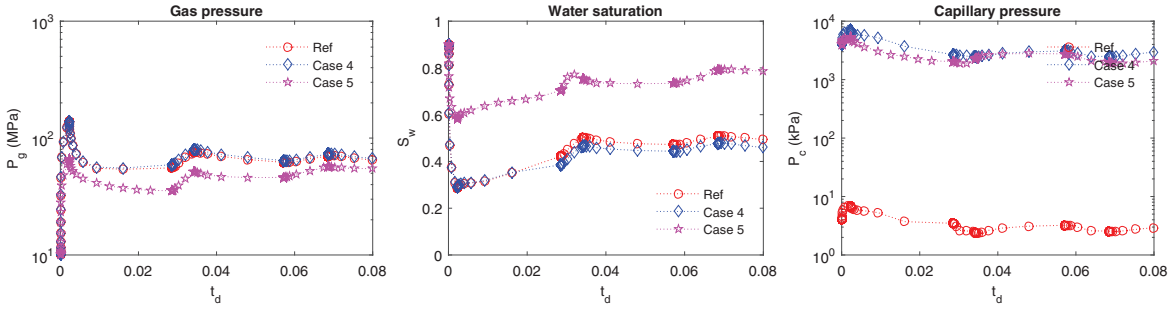

Figure 15: Evolution of gas pressure (left), water saturation (center), and capillary pressure (right) at the monitoring point for Cases 4 and 5.

6.3. *Effect of relative permeability*

We take a different model of gas relative permeability while keeping the same model of capillary pressure (i.e., Case 6). In this case, we still obtain numerically stable results of hysteretic capillary pressure and relative permeability for cyclic drainage and imbibition processes, as shown in Figure 16. In particular, the relative permeability of Case 6 is mostly higher than that of the reference case. As a result, as shown in the center of Figure 17, water movement in this case is faster than that of the reference case. From Figure 17, we find the different distributions of water saturation and capillary pressure between Case 6 and the reference case. At the monitoring point, the two different models of relative permeability also yield different evolutions of gas pressure, water saturation, and capillary pressure (Figure 18).

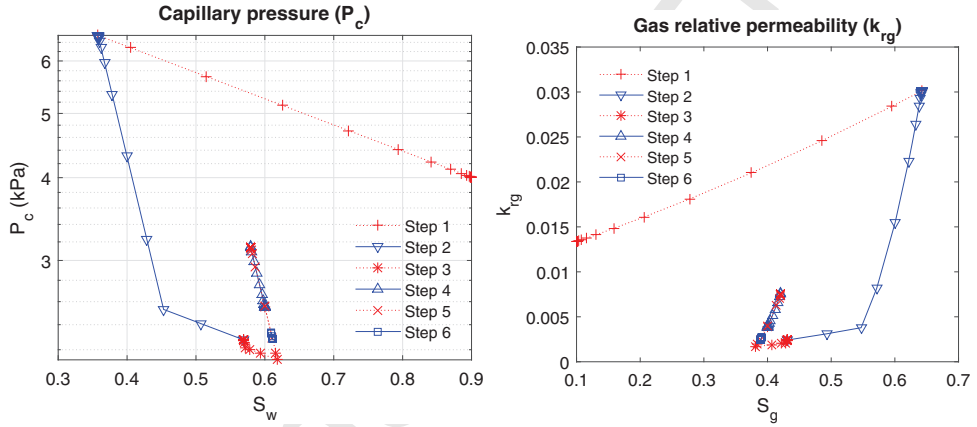

Figure 16: Evolution of capillary pressure (left) and gas relative permeability (right) for Case 6.

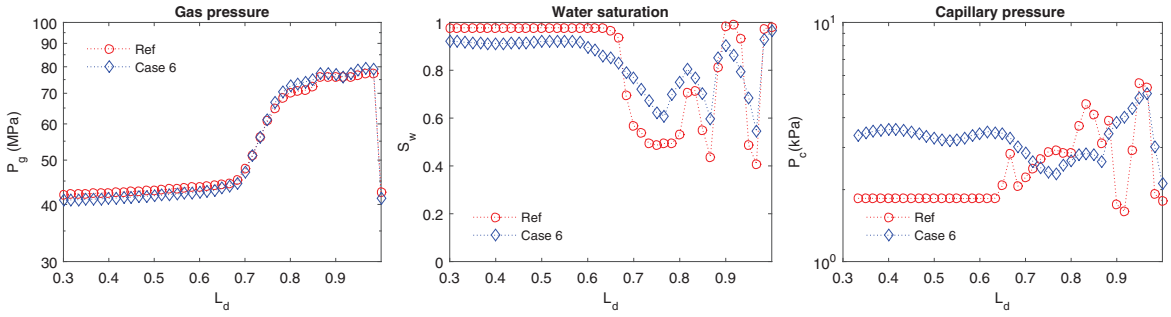

Figure 17: Distribution of gas pressure (left), water saturation (center), and capillary pressure (right) after Step 6 for Case 6.

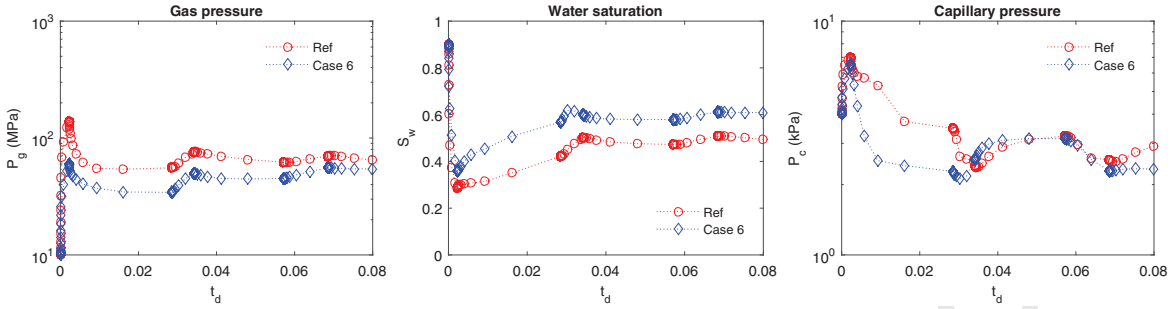

Figure 18: Distribution of gas pressure (left), water saturation (center), and capillary pressure (right) after Step 6 for Case 6.

6.4. Computational performance

We compare computational costs of the test cases in terms of the total number of Newton's iteration during simulation, shown in Table 5. We define the convergence criterion based on the relative error, $\epsilon_r = r_J^k/m_J^k$, where r_J^k and m_J^k are the residual and mass of phase J at the kth iteration, respectively [25]. We then take tolerance of 10^{-5} for all test cases in this study, and convergence for the Newton-Raphson method is achieved every time step when $|\epsilon_r| \leq 10^{-5}$ each gridblock. No significant difference of iteration was found among the cases except Case 6, where n_g=2 while n_g=4 for the other cases. It is natural that different exponents of the relative permeability model (Case 1 and Case 6) induce different computational costs. In particular, the iteration number of Case 1 is lower than that of Case 3, which implies that the hysteresis modeling of this study does not cause significant extra computational cost. It is worth noting that the return mapping algorithm used in this study is linear. Thus, computational efforts between with and without hysteresis are almost the same.

Table 5: Total number of Newton's iteration during simulation

	Case 1	Case 2	Case 3	Case 4	Case 5	Case 6
Iteration	413	430	431	413	442	347

7. Conclusions

We analyzed applicability of the plasticity theory to the modeling for hysteretic capillarity and relative permeability in the two-phase flow system. This modeling approach is generic, not being restricted to a specific type of equations for capillary pressure and relative permeability. We can also make use of systematic algorithms

and mathematical rigorousness previously developed in computational plasticity. We performed mathematic analysis and found that the plasticity-based modeling provides contractivity and B-stability. This implies that the modeling scheme is numerically stable even for many cyclic drainage-imbibition processes. The numerical experiments supported the mathematic analysis, showing that the proposed modeling approach is robust and rigorous, which can track residual saturation dynamically. We identified the importance of hysteresis modeling from numerical results, which showed substantial differences between with and without hysteresis modeling for strong hysteretic capillary pressure and relative permeability.

8. Acknowledgements

This study was supported by the U.S. Department of Energy (Award No. DE-FE0028973), Methane Hydrate Program.

References

[1] A. Firoozabadi, J. Hauge, Capillary pressure in fractured porous media, Journal of Petroleum Technology 42 (1990) 784–791.

[2] S. M. Hassanizadeh, W. G. Gray, Thermodynamic basis of capillary pressure in porous media, Water Resources Research 29 (1993) 3389–3405.

[3] Y. Guan, D. G. Fredlund, Use of the tensile strength of water for the direct measurement of high soil suction, Canadian Geotechnical Journal 34 (1997) 604–614.

[4] P. Binning, M. A. Celia, Practical implementation of the fractional flow approach to multiphase flow simulation, Advances in Water Resources 22 (1999) 461–478.

[5] S. M. Hassanizadeh, M. A. Celia, H. K. Dahle, Dynamic effect in the capillary pressure-saturation relationship and its impact on unsaturated flow, Vadose Zone Journal 1 (2002) 38–57.

[6] R. Juanes, E. J. Spiteri, F. M. Orr, Impact of relative permeability hysteresis on geological co2 storage, Water Resources Research 42 (2006) W12418.

[7] A. Cihan, J. Birkholzer, T. H. Illangasekare, A modeling approach to represent hysteresis in capillary pressure-saturation relationship based on fluid connectivity in void space, Water Resources Research 50 (2014) 119–131.

[8] J. B. Kool, J. C. Parker, Development and evaluation of closed-form expressions for hysteresis soil hydraulic properties, Water Resources Research 23 (1987) 105–114.

[9] R. J. Lenhard, J. C. Parker, J. J. Kaluarachchi, Comparing simulated and experimental hysteretic two-phase transient fluid flow phenomena, Water Resources Research 27 (1991) 2113–2124.

[10] J. E. Killough, Reservoir simulation with history-dependent saturation fuctions, SPE Journal 16 (1976) 37–48.

[11] C. Doughty, Modeling geologic storage of carbon dioxide: Comparison of non-hysteretic and hysteretic characteristic curves, Energy Conversion and Management 48 (2007) 1768–1781.

[12] M. Nuth, L. Laloui, Advances in modeling hysteretic water retention curve in deformable soils, Computers and Geotechnics 35 (2008) 835–844.

[13] D. M. Pedroso, D. J. Williams, A novel approach for modelling soil–water characteristic curves with hysteresis, Computers and Geotechnics 37 (2010) 374 – 380.

[14] J. C. Simo, T. J. R. Hughes, Computational inelasticity, Springer, Heidelberg, 1998.

[15] K. Aziz, A. Settari, Petroleum Reservoir Simulation, Elsevier, London, 1979.

[16] O. Coussy, Mechanics of porous continua, John Wiley and Sons, Chichester, England, 1995.

[17] F. Armero, Formulation and finite element implementation of a multiplicative model of coupled poro-plasticity at finite strains under fully saturated conditions, Computer Methods in Applied Mechanics and Engineering 171 (1999) 205–241.

[18] O. Coussy, Poromechanics, John Wiley and Sons, Chichester, England, 2004.

[19] J. Kim, A new numerically stable sequential algorithm for coupled finite-strain elastoplastic geomechanics and flow, Computer Methods in Applied Mechanics and Engineering 335 (2018) 538–562.

[20] J. Simo, Nonlinear stability of the time-discrete variational problem of evolution in nonlinear heat conduction, plasticity and viscoplasticity, Computer Methods in Applied Mechanics and Engineering 88 (1991) 111–131.

[21] A. Araújo, A note on b-stability of splitting methods, Computing and Visualization in Science 6 (2004) 53–57.

[22] W. H. Hundsdorfer, M. L. Splijer, A note on b-stability of runge-kutta methods, Numerische Mathematik 36 (1981) 319–331.

[23] J. Kim, H. A. Tchelepi, R. Juanes, Rigorous coupling of geomechanics and multiphase flow with strong capillarity, SPE Journal 18 (2013) 1123–1139.

[24] I. Romero, Thermodynamically consistent time-stepping algorithms for non-linear thermomechanical systems, International Journal for Numerical Methods in Engineering 79 (2009) 706–732.

[25] K. Pruess, C. Oldenburg, G. Moridis, TOUGH2 User's Guide, Version 2.0. Report LBNL-43134, Lawrence Berkeley National Laboratory, 1999.

[26] R. H. Brooks, A. T. Corey, Hydraulic properties of porous media, Hydrology Papers 3, Colorado State University, Fort Collins, 1964.

[27] van Genuchten, A closed-form equation for predicting the hydraulic conductivity of unsaturated soils, Soil Science Society of America Journal (1980) 892–898.

[28] R. J. Lenhard, J. C. Parker, S. Mishra, On the correspondence between brooks-corey and van genuchten models, Journal of Irrigation and Drainage Engineering 115 (1989) 744–751.

Declaration of interests

☒ The authors declare that they have no known competing financial interests or personal relationships that could have appeared to influence the work reported in this paper.

☐The authors declare the following financial interests/personal relationships which may be considered as potential competing interests: